Pattern-integrated interference lithography: single-exposure fabrication of photonic-crystal structures

Guy M. Burrow, Matthieu C. R. Leibovici, and Thomas K. Gaylord*

School of Electrical and Computer Engineering, Georgia Institute of Technology, 777 Atlantic Drive NW, Atlanta, Georgia 30332-0250, USA

*Corresponding author: tgaylord@ece.gatech.edu

Received 14 March 2012; accepted 21 April 2012;
posted 27 April 2012 (Doc. ID 164525); published 12 June 2012

Multibeam interference represents an approach for producing one-, two-, and three-dimensional periodic optical-intensity distributions with submicrometer features and periodicities. Accordingly, interference lithography (IL) has been used in a wide variety of applications, typically requiring additional lithographic steps to modify the periodic interference pattern and create integrated functional elements. In the present work, pattern-integrated interference lithography (PIIL) is introduced. PIIL is the integration of superposed pattern imaging with IL. Then a pattern-integrated interference exposure system (PIIES) is presented that implements PIIL by incorporating a projection imaging capability in a novel three-beam interference configuration. The purpose of this system is to fabricate, in a single-exposure step, a two-dimensional periodic photonic-crystal lattice with nonperiodic functional elements integrated into the periodic pattern. The design of the basic system is presented along with a model that simulates the resulting optical-intensity distribution at the system sample plane where the three beams simultaneously interfere and integrate a superposed image of the projected mask pattern. Appropriate performance metrics are defined in order to quantify the characteristics of the resulting photonic-crystal structure. These intensity and lattice-vector metrics differ markedly from the metrics used to evaluate traditional photolithographic imaging systems. Simulation and experimental results are presented that demonstrate the fabrication of example photonic-crystal structures in a single-exposure step. Example well-defined photonic-crystal structures exhibiting favorable intensity and lattice-vector metrics demonstrate the potential of PIIL for fabricating dense integrated optical circuits.

OCIS codes: 070.0070, 110.3925, 220.2945, 220.3740, 220.4000, 230.5298.

1. Introduction

Multibeam interference (MBI) provides the ability to form a wide variety of periodic optical-intensity distributions at the microscale and nanoscale in one, two, and three dimensions. Accordingly, interference lithography (IL) has the potential to impact a wide variety of application areas [1,2] including nanoelectronics [3–5], photonic crystals (PCs) [6–8], metamaterials [9,10], subwavelength structures [11–15], optical trapping [16–18], and biomedical structures [19–21]. Numerous periodic and quasi-periodic patterns with specific space-group symmetries and motif geometries are possible by careful selection of individual beam amplitudes, polarizations, and wave vector configurations [22–25]. These same parameters also enable the optimization of the contrast of the periodic distribution, providing lithographically useful patterning possibilities [26–29]. As such, several optical configurations and lithographic techniques have been developed that incorporate IL [5,30–34], providing the potential for simple, rapid, wafer-scale, and low-cost fabrication [35,36]. In fact, a recent economic assessment of various lithography choices concluded that a double-exposure technique, optimized by the

1559-128X/12/184028-14$15.00/0

use of IL, may be the best choice for low to medium volume production [37]. However, additional research is needed to make IL a preferred component of higher volume commercial fabrication.

Recently, IL was combined with traditional mask-based photolithography techniques, allowing for interference patterning incorporating nonperiodic mask-defined elements in a positive photoresist [38]. In this method, once the periodic pattern was recorded in the photoresist through multiple two-beam exposures, a final exposure was made with a third beam, illuminating a mask on or in close proximity to the sample to create the functional elements. More recently, a five-beam diffractive-grating mask was modified to include an amplitude mask with the central beam. Using this method, a single exposure was used, for the first time, to produce a four-beam interference pattern incorporating a single low-spatial-frequency mask element [39].

A comparison of the combined techniques used to fabricate nonperiodic functional elements in an MBI-defined periodic lattice is provided in Table 1. While the first five techniques listed in Table 1 offer the ability to fabricate high-spatial-frequency integrated functional elements, they are all prohibitively expensive and are based on time-consuming sequential fabrication methods to define the functional elements, precluding their use in commercial production. When projection lithography is used to define the functional elements, as demonstrated in interference-assisted lithography, large-area patterning becomes possible, thereby reducing the fabrication time [5]. However, the requirement for multiple exposures makes this technique too expensive for large-volume production [37]. With the recent demonstration of IL combined with proximity or contact lithography in a single-exposure step [39], commercially cost-effective fabrication seems possible. Unfortunately, while contact lithography offers high resolution, mask damage results in low yield, making this method too costly for commercial production applications [40]. While proximity lithography reduces the risk of mask damage, this method is not capable of fabricating the full range of high-spatial frequency integrated functional elements, with a typical resolution, or smallest feature size that can be recorded in a photoresist, limited to 2–4 μm [40].

A new lithographic method is needed to integrate a nonperiodic functional element pattern within an MBI-defined periodic lattice in a single-exposure step, thereby reducing the complexity, fabrication time, and associated costs, making this combination a potential option for large-volume commercial fabrication. Pattern-integrated interference lithography (PIIL) is presented to address this need. PIIL is the integration of superposed pattern imaging with IL. The result is an optical-intensity distribution composed of an MBI-defined periodic lattice modified by an integrated mask pattern image to form functional elements. In the present work, a pattern-integrated interference exposure system (PIIES) implements the PIIL methodology by incorporating a projection-imaging capability in a novel three-beam interference configuration, enabling the single-exposure fabrication of a two-dimensional periodic photonic-crystal lattice with nonperiodic functional elements integrated into the periodic pattern [41,42]. After a description of the basic system design and functionality, a model is presented to simulate the optical-intensity distribution at the PIIES sample plane. The model is then used to evaluate the characteristics of the resulting PC structure with new intensity and lattice-vector metrics that differ markedly from those used in traditional photolithographic imaging systems. As a demonstration of PIIL, an experimental PIIES configuration is used to fabricate representative PC structures in a single-exposure step. Both simulations and experimental results confirm the potential of PIIL as a method for fabricating dense integrated optical circuits.

2. Pattern-Integrated Interference Exposure System

A conceptual three-beam PIIES configuration is depicted in Fig. 1 [41,43]. To describe the PIIES functionality, we begin with the basic wave vector configuration required to produce a square-lattice interference pattern. Figure 1(a) depicts three plane waves generated from a common source, represented by wave vectors $\mathbf{k}_1$, $\mathbf{k}_2$, and $\mathbf{k}_3$, which intersect at the sample plane located at the x-y plane, where the three beams interfere to produce a periodic optical-intensity distribution with a square translational symmetry defined by principal lattice vectors,

Table 1. Comparison of Combined Techniques to Fabricate Nonperiodic Functional Elements in an MBI-Defined Periodic Lattice

	Technique Characteristics			
Functional Element Fabrication Technique	Fast?	Single-Exposure?	Cost-Effective?	High-Spatial-Frequency Integrated Functional Elements?
Electron beam lithography [32]	No	No	No	Yes
Focused ion beam [34]	No	No	No	Yes
Direct laser writing [31]	No	No	No	Yes
Atomic force microscope nano-indentation [33]	No	No	No	Yes
Multi-photon polymerization [30]	No	No	No	Yes
Projection lithography [5]	Yes	No	No	Yes
Contact lithography [38,39]	Yes	Yes	No	Yes
Proximity lithography [38,39]	Yes	Yes	Yes	No
Pattern-integrated interference lithography	Yes	Yes	Yes	Yes

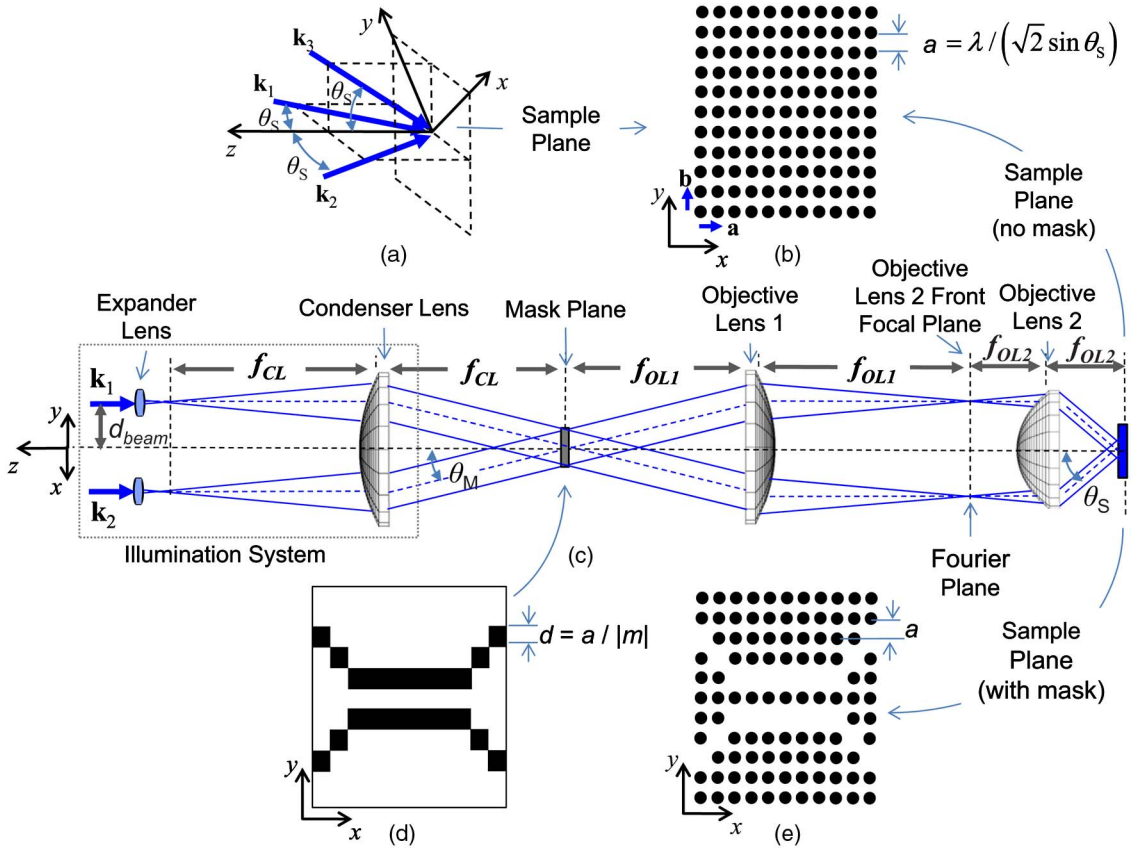

Fig. 1. (Color online) Three-beam pattern-integrated interference exposure system (PIIES) [41]. (a) The configuration of wave vectors k_1, k_2, and k_3 produce (b) a square-lattice interference pattern with a lattice constant $a = \lambda/(\sqrt{2}\sin\theta_s)$; (c) a ray trace depicts the propagation of k_1 and k_2 through the PIIES optical configuration (k_3 is not shown for clarity but is parallel to k_1 and k_2 and lies out of the plane of the page). The interfering beams are collimated and intersect at the sample plane forming a uniform square-lattice pattern. (d) A functional-element amplitude mask is placed at the mask plane with mask features sizes of $d = a/|m|$, where m is the magnification due to the compound objective lens; (e) the result is an optical-intensity distribution of an integrated nonperiodic functional element in an all-surrounding high-spatial-frequency periodic square lattice, enabling single-exposure fabrication of a PC device, such as a PC waveguide coupler [44].

a and **b**, as depicted in Fig. 1(b). The periodicity, or lattice constant a, of the square lattice is given by

$$a = \lambda/\left(\sqrt{2}\,\sin\,\theta_s\right), \tag{1}$$

where λ is the wavelength of the source and θ_s is the common angle of incidence of the interfering beams with respect to the sample-plane normal. To implement this wave vector configuration in the PIIES, Fig. 1(c) depicts a ray trace of $\mathbf{k}_1$ and $\mathbf{k}_2$ ($\mathbf{k}_3$ is not shown for clarity but is parallel to $\mathbf{k}_1$ and $\mathbf{k}_2$ and lies out of the plane of the page). Initially, the multiple beams propagate parallel to the optical axis of the system at a common beam displacement d_{beam}. To achieve the desired interference patterning capability, the PIIES configuration incorporates two unique design considerations. First, the expander, condenser, and first objective lenses are positioned such that each beam is focused at the front focal plane of the second objective lens. This ensures that each interfering beam is collimated at the exit of the objective lens, producing a uniform-periodic interference pattern at the sample plane. Second, d_{beam} is adjusted to provide a specific incidence angle at the sample plane θ_s to achieve a desired lattice constant as given by Eq. (1). It should be noted that more complex optical systems may be systematically designed to produce collimated interfering beams while improving the integrated projection-imaging capability. However, in the work presented here, a 6f configuration is chosen to satisfy the collimating requirements, facilitate modeling, and provide a relatively simple low-cost prototype to demonstrate the PIIL concept.

While the multiple beams, expander lenses, and condenser lens are specifically positioned to produce collimated interfering beams at the sample plane, these same components also serve as the illumination system for the integrated PIIES projection capability as depicted in Fig. 1(c). In the present configuration, the PIIES mask plane is collocated at the condenser lens back focal plane where the three expanded beams intersect, providing coherent multibeam off-axis illumination of an object such as the amplitude mask depicted in Fig. 1(d). The purpose of this mask is two-fold. First, the transparent areas of the mask allow the multiple beams to pass through

and form the desired interference pattern at the sample plane. Second, the opaque areas of the mask block and diffract the illuminating beams, portions of which are collected by the objective lenses and focused at the sample plane. These projected mask elements effectively block the multiple interfering beams at the sample plane, thereby preventing or altering the formation of portions of the interference pattern at areas corresponding to the functional elements defined by the mask features with dimensions $d = a/|m|$, where m is the magnification due to the compound objective lens. The result is an optical-intensity distribution containing integrated nonperiodic functional elements in an all-surrounding high-spatial-frequency MBI-defined periodic pattern. This distribution may, in turn, be recorded in a photoresist, in a single-exposure step, to form functional devices, such as the PC waveguide coupler depicted in Fig. 1(e) [44].

The illumination system presented here differs from the traditional Köhler illumination in three subtle but important ways. First, the PIIES illumination system is positioned so that the mask plane is located at the condenser-lens back focal plane. With traditional Köhler illumination, the mask is typically placed closer to the condenser lens [45]. Second, the multiple illuminating beams are derived from point sources located at the back focal plane of the expander lenses, resulting in approximately coherent off-axis illumination of the mask by each beam. In a Köhler illumination scheme, the diameter of the source is varied to obtain corresponding degrees of partial coherence, where the source may be thought of as a collection of point sources emanating from within the diameter of the source. Finally, the PIIES illumination system is adjusted such that the multiple beams are focused at the objective lens front-focal plane to achieve collimated beams at the sample plane. With Köhler illumination, the source is focused at the objective lens entrance pupil [45]. For a single on-axis source, the Köhler illumination produces a partially coherent beam at the sample plane for each point within the diameter of the source. This results in numerous interference fringes for each beam pair, varying in periodicity, orientation, and translational position. These interference fringes superpose and average to an approximately uniform intensity distribution. In fact, this is a desired result in traditional Köhler illumination. These subtle differences incorporated into the illumination scheme enable the PIIES to form an optical-intensity distribution that is the combination of a periodic pattern (formed by the multiple interfering beams) and integrated nonperiodic functional elements (formed by the mask projection).

3. System Modeling

While both MBI and projection imaging have been modeled separately, a new model is required for them to be combined into the PIIES aerial optical-intensity distribution. For linearly polarized beams, the time-average optical-intensity distribution at the PIIES sample plane is given by

$$\begin{aligned} I_T(\mathbf{r}) = I_0(\mathbf{r})\{1 &+ V_{12}(\mathbf{r})\cos[(\mathbf{k}_2 - \mathbf{k}_1)\cdot\mathbf{r}] \\ &+ V_{13}(\mathbf{r})\cos[(\mathbf{k}_3 - \mathbf{k}_1)\cdot\mathbf{r}] \\ &+ V_{23}(\mathbf{r})\cos[(\mathbf{k}_3 - \mathbf{k}_2)\cdot\mathbf{r}]\}, \end{aligned} \tag{2}$$

where the constant intensity term $I_0(\mathbf{r})$ and $V_{ij}(\mathbf{r})$ interference coefficients are defined as

$$I_0(\mathbf{r}) = \sum_{i=1}^{3}\frac{1}{2}E_i(\mathbf{r})^2 \quad \text{and} \quad V_{ij}(\mathbf{r}) = \frac{E_i(\mathbf{r})E_j(\mathbf{r})(\hat{\mathbf{e}}_i\cdot\hat{\mathbf{e}}_j)}{I_0(\mathbf{r})}, \tag{3}$$

where $E_i(\mathbf{r})$, $\hat{\mathbf{e}}_i$, and $\mathbf{k}_i$ are the electric-field amplitude, polarization vector, and wave vector of the ith beam, respectively [46].

If no mask is present in the PIIES configuration of Fig. 1(c), the constant intensity term and interference coefficients become simple scalar values, $I_0$and V_{ij} and Eq. (2) simplifies to the familiar equation for the interference pattern formed by three linearly polarized monochromatic plane waves. However, when a mask is placed at the mask plane, the constant intensity term and interference coefficients become complex as defined by Eq. (3). To understand the effects of integrating a pattern mask, the PIIES compound objective lens of Fig. 1(c) is arranged as a $4f$ optical system that can be modeled using Fourier optics. In this configuration, the complex electric field for the ith beam at the sample plane can be expressed as

$$E_i(x,y) = \mathcal{F}^{-1}[M_i(f_x,f_y)P(f_x,f_y)], \tag{4}$$

where $\mathcal{F}^{-1}$ is the inverse Fourier transform, f_x and f_y are the spatial frequencies, $M_i(f_x,f_y)$ is the electric field at the Fourier plane, and $P(f_x,f_y)$ is the objective-lens pupil function [47].

A. Mask Function

For a thin binary or grayscale complex amplitude mask, illuminated by a single coherent on-axis beam, the electric field at the Fourier plane is given by

$$\begin{aligned} M(f_x,f_y) &= \iint t(x,y)\exp[-i2\pi(f_x x + f_y y)]\mathrm{d}x\mathrm{d}y \\ &= \mathcal{F}[t(x,y)], \end{aligned} \tag{5}$$

where $t(x,y)$ is the amplitude transmittance of the mask and $\mathcal{F}$ is the Fourier transform [47]. For on-axis mask illumination, the amplitude pattern at the Fourier plane is centered at the origin. However, in the PIIES configuration, three off-axis beams illuminate the mask at a common incidence angle θ_M as illustrated in Fig. 1(c). As a result, the amplitude patterns associated with each beam are shifted in spatial frequency from the origin by an amount

$$(f'_{x,i}, f'_{y,i}) = \left(\frac{\sin\theta_M \cos\varphi_i}{\lambda}, \frac{\sin\theta_M \sin\varphi_i}{\lambda}\right), \quad (6)$$

where φ_i is the azimuthal angle of the ith beam [47]. As a consequence, each off-axis beam creates a unique complex electric field at the Fourier plane, $M_i(f_x - f'_{x,i}, f_y - f'_{y,i})$, that results in unique complex electric fields, $E_i(x,y)$, for each beam at the sample plane as defined by Eq. (4). The electric field amplitude, $E_i(\mathbf{r})$ for each beam is then the magnitude of the complex electric field.

B. Pupil Function

For an aberration-corrected lens, the ideal pupil function describes the light collected and transmitted by the objective lens and is defined as

$$P(f_x, f_y) = \begin{cases} 1, & \text{if } \sqrt{f_x^2 + f_y^2} < \frac{CA_2/2}{\lambda f_2} \\ 0, & \text{if } \sqrt{f_x^2 + f_y^2} > \frac{CA_2/2}{\lambda f_2} \end{cases}, \quad (7)$$

where CA_2 is the clear aperture and f_2 is the focal length of the second objective lens [48].

When the magnification m of the optical system is considered, the angles of incidence in the mask plane and in the sample plane are not the same for every spatial frequency. Consistent with energy conservation, an obliquity factor must be included in the pupil function. In the spatial frequency domain, the obliquity factor can be expressed as [45]

$$O(f_x, f_y) = \left[\frac{1 - m^2\lambda^2(f_x^2 + f_y^2)}{1 - \lambda^2(f_x^2 + f_y^2)}\right]^{\frac{1}{4}}. \quad (8)$$

Next, wave front aberrations in the optical system may be included by using the 37-term Zernike polynomial $W(x,y)$. The fringe Zernike coefficients for this polynomial for the compound objective lens may be found using Zemax [49] optical system design software. In the spatial-frequency domain, the wave front aberrations can be expressed as [47]

$$Z(f_x, f_y) = \exp\left[i\frac{2\pi}{\lambda} W(\lambda f_2 f_x, \lambda f_2 f_y)\right]. \quad (9)$$

The total pupil function of the PIIES is then given by

$$P(f_x, f_y) = P_{\text{ideal}}(f_x, f_y) O(f_x, f_y) Z(f_x, f_y). \quad (10)$$

Together, the mask and pupil functions provide a full scalar model using Eq. (4). However, the current model does not include full polarization considerations as it has been demonstrated that the nonparaxial scalar model remains applicable for a numerical aperture NA (sine of the half apex angle of the acceptance cone in air) up to approximately 0.6 [50]. With a maximum NA of 0.62 for objective lens 2, polarization effects are not included here, and individual beam polarizations are assumed to remain linear throughout the optical system. Full polarization considerations will be the subject of future work as larger NAs are considered.

C. Aerial Optical-Intensity Distribution Simulation

Using Eq. (2) and representative optical system parameters described in Appendix A, the aerial optical-intensity distribution at the PIIES sample plane was simulated using MATLAB [51] as depicted in Fig. 2. Figure 2(a) illustrates the interference pattern of three beams with no mask present, matching the predictions of Stay *et al.* for a $p4m$ plane-group symmetry [29]. When the functional-element mask of Fig. 1(d) is placed at the mask plane and illuminated by a single off-axis beam, the resulting normalized projected aerial intensity distribution at the sample plane is depicted in Fig. 2(b). Despite diffraction effects and lens aberrations, the projected functional-element image remains well defined. Figure 2(c) shows the complete normalized optical-intensity distribution at the sample plane when the mask is illuminated by all three off-axis interfering beams. Here, the combination of MBI and the projected functional-element mask pattern produces an overall distribution that very closely resembles the desired pattern for the example PC waveguide coupler depicted in Fig. 1(e). A closer inspection of Fig. 2(c) reveals some slight amplitude variations and lattice-point distortions near the functional element. Accordingly, a discussion of PIIL perfomance metrics follows.

4. Pattern Metrics

In optical lithography for micro-electronic and nano-electronic circuitry, the conventional quality metrics for the resulting pattern include (1) the minimum feature size [often the half pitch of a dynamic random access memory (DRAM) cell], (2) distortion (also called tilt) (magnification varying with distance from the axis of the optical system producing placement error as a function of field position), (3) corner rounding, (4) line edge roughness (deviations from a smooth sidewall of a feature in the depth direction), (5) sidewall angle (angle of photoresist sidewall), (6) presence of an "open" at a location where two conductors should be connected (represents a fatal fault), and (7) presence of a "short" where two conductors should be separated (also a fatal fault). These metrics are very appropriate for conventional integrated electronic circuits where the electrical characteristics are of paramount importance.

However, in optical integrated circuits, a waveguide, coupler, resonator, or modulator functions satisfactorily if it meets or exceeds its operational performance specifications. In general, there is a gradual degradation of optical device performance with fabrication errors. An optical waveguide, for example, may transmit light in a completely satisfactory manner even though there are refractive index variations within the waveguiding region due to nonideal photolithography. On the other hand, specific

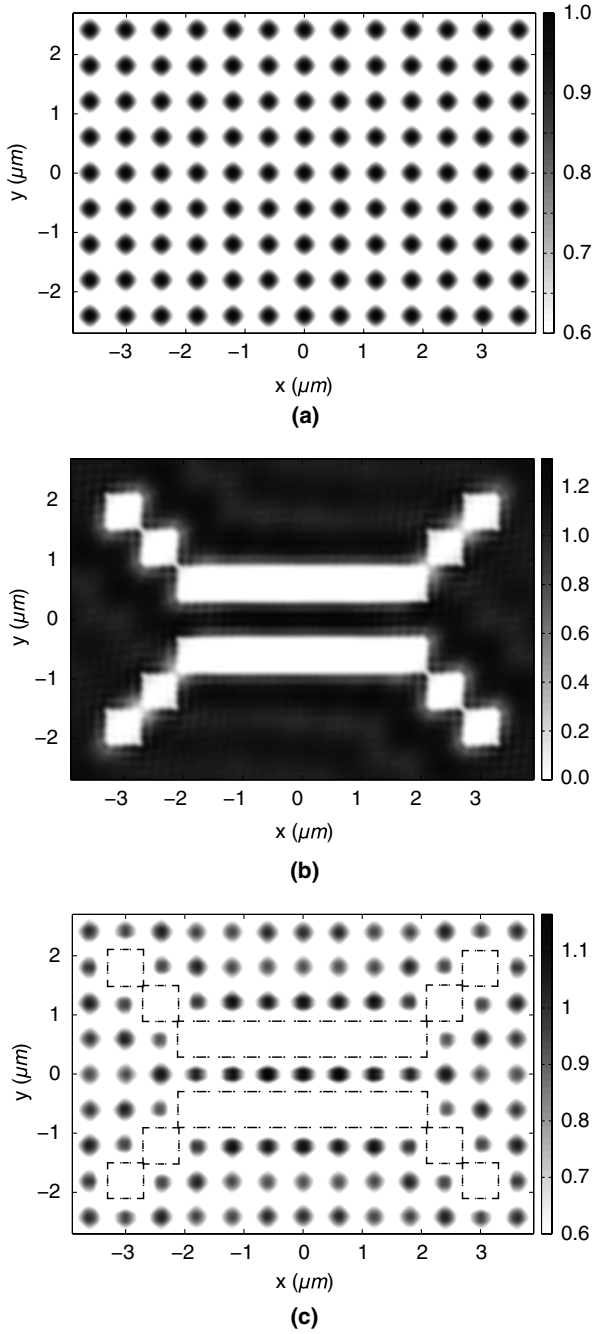

Fig. 2. Simulated normalized aerial optical-intensity distribution at the PIIES sample plane. (a) With no mask present, the normalized intensity plot depicts a uniform periodic three-beam interference pattern; (b) when a mask is illuminated by a single off-axis beam, the projected aerial intensity distribution at the sample plane is defined by the mask pattern; (c) when the mask is illuminated by all three off-axis interfering beams, the simulated optical-intensity distribution at the sample plane includes interference and projection patterning (outlined by a dashed line), allowing for the single-exposure formation of a PC device.

patterns of low-level refractive index changes may produce unacceptably large scattering losses in the waveguide. Figure 3 depicts the simulated PIIES optical-intensity distribution for the PC waveguide coupler presented in Fig. 2(c) with detailed views of several individual lattice points. The first motif depicted in Fig. 3(b), representing an unperturbed lattice point, is obtained when no mask is present or alternatively at locations in the optical-intensity distribution that are sufficiently removed from functional elements. Figures 3(c) and 3(d) represent motifs in close proximity to the functional element, yet these motifs are still relatively unperturbed. In some cases, the projected functional element has a noticeable effect on some individual motifs immediately adjacent to the functional element as depicted in Figs. 3(e)–3(g).

While the qualitative observations provided by Fig. 3 are instructive, quantitative measures will become important and should be defined to enable specifications and tolerances on the design, fabrication, and performance of functional optical integrated circuits created using PIIL. Photonic-crystal device and circuit development is still a relatively young field. Correspondingly there are a myriad of additional issues to be addressed. At this early stage of progress, it is particularly important to define a relatively complete set of pattern metrics in terms

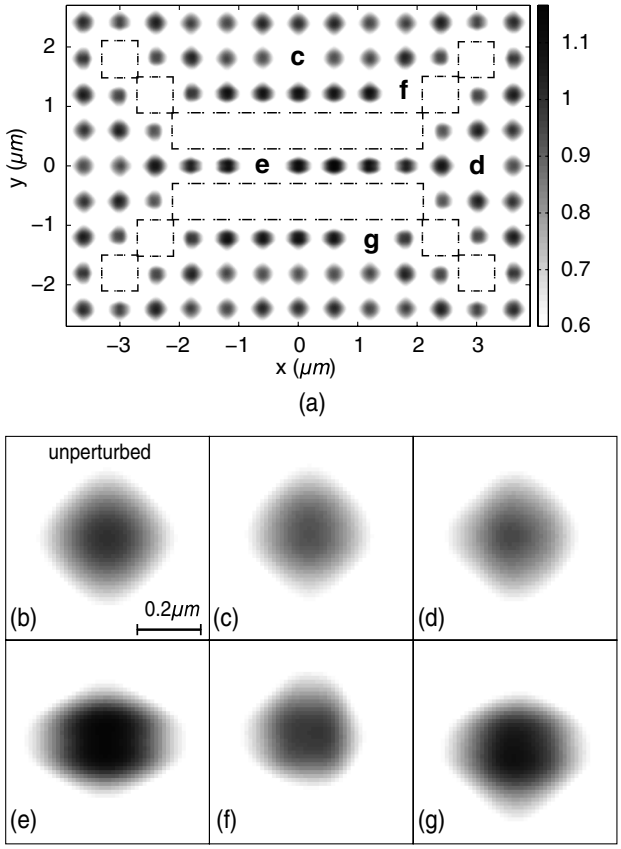

Fig. 3. Simulated PIIES aerial optical-intensity distribution for a PC waveguide coupler. (a) The normalized intensity depicts a projected functional element (outlined by a dashed line) that prevents the formation of interference lattice points to define a PC waveguide coupler in a single exposure; (b) an unperturbed PC lattice point in the absence of a pattern mask forms a motif with $p4m$ plane group symmetry; (c), (d) most motifs in close proximity to the functional element remain relatively unperturbed; while (e)–(g) the projected functional element has a noticeable effect on some of the PC motifs immediately surrounding PC device.

of the aerial optical-intensity distribution being produced. These metrics can then be extended in a straightforward manner to the subsequent (1) developed photoresist pattern characteristics and then to the (2) fabricated device characteristics. As with the electronic metrics, statistical distributions of these optical pattern metrics would provide an overall description of the quality of a resulting pattern and aid in the design and optimization of lithographically useful PIIL patterning.

A. Intensity Performance Metrics

The intensity at various positions within the photonic-crystal device pattern needs to be quantified. To facilitate comparison, the intensity values are normalized to the intensity at a lattice point in the unperturbed periodic lattice (no functional elements present) as depicted in Fig. 3(b). In the PIIES, this periodic pattern would be produced with the mask absent (flood exposure or open frame exposure) so that only the periodic pattern exists (no functional elements). Even though in practice the mask can be a binary or gray-scale amplitude and/or phase mask, for simplicity it will be taken here to be a binary amplitude mask for the purpose of defining the intensity metrics below.

Mask-Unaltered-Lattice-Unit-Cell-Intensity Metrics, In1–In4: These metrics give the normalized intensities at locations within the unit cells where (based on the mask pattern) the periodic PC pattern should be unaltered.

Mask-Altered-Lattice-Unit-Cell-Intensity Metrics, In5–In8: These metrics give the normalized intensities at locations within the unit cells where (based on the mask pattern) the intensity should be zero, corresponding to functional elements.

The eight intensity metrics, In1–8, are defined in Table 2. From these metrics, a wide range of contrast ratios can therefore be defined as needed.

B. Lattice-Vector Performance Metrics

Lattice-vector performance metrics provide information about variations in the fundamental lattice vectors, which may become "distorted" due to a nearby functional element.

Mask-Unaltered-Lattice-Vector Metrics, LV1–LV8: These metrics give the normalized lengths and angular deviations of the fundamental lattice vectors in the principal axis directions, **a** and **b**, as depicted in Fig. 1(b). The metrics are referenced to the lengths and angles of the fundamental lattice vectors in the unperturbed (no functional elements) PC lattice. The eight lattice-vector metrics, LV1–LV8, are defined in Table 2.

For the example PC waveguide coupler, the simulated maximum and minimum pattern metric locations and values are depicted in Fig. 4. The values for metrics In1–In4 reveal that the PC lattice point intensities remain very close to the desired unperturbed values with maximum perturbations of 20% or less for this case. One notable deviation is In7 at a value of 0.20 representing an unwanted, yet significantly attenuated lattice point within the functional element. This value is well below the levels of the surrounding PC lattice points, suggesting that normal lithographic processing techniques would prevent the formation of lattice points within the functional element. For example, the intensity plot of Fig. 3 only depicts normalized intensity values above 0.6, well above the In7 value of 0.20.

The lattice-vector metrics given in Fig. 4 also show minimal effects of the pattern mask with normalized vector lengths varying by less than 6% and angular deviations of less than 5 deg at locations near the functional element. To gain a better appreciation for the lattice-vector perturbations across the entire optical-intensity distribution, Fig. 5 provides a comprehensive view of the lattice-vector metrics distributed between adjoining PC lattice points with normalized lattice-vector length perturbations (LV1–LV4) depicted in Fig. 5(a) and angular deviations (LV5–LV8) depicted in Fig. 5(b).

Beyond the amplitude and lattice-vector metrics presented here, the shapes and therefore the symmetries of the unit cells in the PC pattern will vary due to deviations from the unperturbed lattice geometry. For example, the unperturbed circular motifs of an original square or hexagonal symmetry lattice will become altered when a functional element mask is introduced as depicted in Figs. 3(e)–3(g). An ideal square lattice with $p4m$ plane group symmetry may locally become cmm, pmm, $p2$, or $p1$ plane group symmetry. An ideal hexagonal lattice with $p6m$ plane group symmetry may locally become cmm, $p2$ or

Table 2. Intensity and Lattice-Vector Metrics for Unaltered Photonic-Crystal Lattice Points and Altered (Zero Amplitude) Functional Element Locations

Metric Description			
Metric	Pattern Element	Location within Unit Cell	Normalized Intensity
In1	Photonic crystal	Center	Highest
In2			Lowest
In3		Any location	Highest
In4			Lowest
In5	Functional element	Center	Highest
In6			Lowest
In7		Any location	Highest
In8			Lowest
		Lattice-Vector Direction	Normalized Length
LV1	Photonic crystal	**a**	Longest
LV2			Shortest
LV3		**b**	Longest
LV4			Shortest
			Angular Deviation
LV5	Photonic crystal	**a**	Max CCW
LV6			Max CW
LV7		**b**	Max CCW
LV8			Max CW

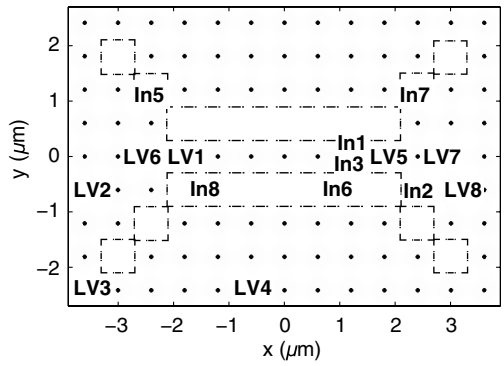

In1=1.16	In2=0.92	In3=1.17	In4=5.03 x 10^{-7}
In5=4.60 x 10^{-3}	In6=9.07 x 10^{-4}	In7=0.20	In8=1.70 x 10^{-5}
LV1=1.06	LV2=0.94	LV3=1.04	LV4=0.94
LV5=3.43°	LV6=-3.43°	LV7=4.67°	LV8=-4.67°

Fig. 4. Simulated PIIES aerial optical-intensity distribution pattern metrics for a PC waveguide coupler. Single points represent the PC lattice with the projected functional element defined by a dashed line. Maximum and minimum locations for the intensity and lattice-vector metrics are labeled with their corresponding values.

$p1$ plane group symmetry. If the motif becomes elliptical, the change can be described generally by its ellipticity. If more accurate models of the motif are required, the distorted motif shape may be defined by a modified super-ellipse equation to describe a shape that varies from an ellipse to a more complex rectilinear geometry as described in previous work [22]. In some situations, this symmetry information may be useful in describing deviations in the resulting optical-intensity pattern, while providing more accurate models to analyze PC device performance.

5. Experimental Configuration and Procedures

To demonstrate basic PIIL functionality and validate design and modeling simulations, the optical configuration depicted in Fig. 1(c) was implemented as illustrated in Fig. 6. A Spectra-Physics argon-ion UV laser was used as the PIIES source, operating at a single-line wavelength of 363.8 nm with an output power of 75 mW. To ensure a high-contrast interference pattern for a wide range of periodic lattice symmetries, a combination of half-wave plates and beam-splitter cubes were used to control individual-beam linear polarizations and amplitudes as reported previously [22,52]. To minimize spherical aberration for on-axis projection patterning, three large-diameter broadband antireflection coated aspheric lens, commercially available from ThorLabs, were used for the condenser and first objective lens (AL100200-B) and the second objective lens (AL7560-A). A four-inch pattern mask was positioned using a three-axis translating pattern-mask mount. Similarly, a two-axis (x and z) translating sample mount was used to position the sample for exposure. As pictured in Fig. 6(b), the experimental configuration included a pre-exposure real-time monitoring capability as reported previously [52] to confirm MBI patterning symmetries, facilitate system alignment, and establish initial focusing of projected pattern-mask features.

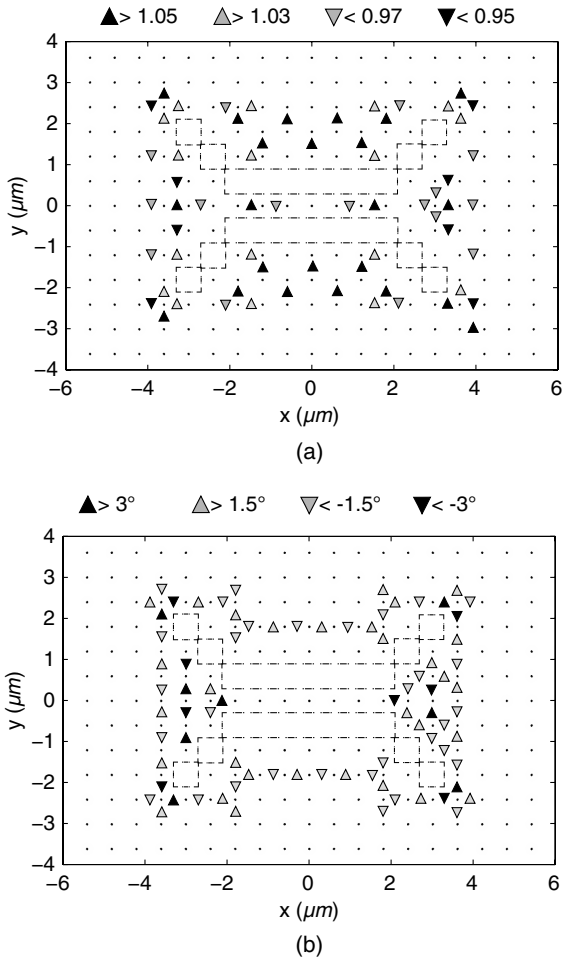

Fig. 5. Simulated PIIES aerial optical-intensity distribution lattice-vector metrics for an example PC waveguide coupler. (a) The normalized lattice-vector lengths vary by 6% or less with (b) angular deviations of less than 5 deg.

A basic lithographic exposure procedure was used to record the PIIES optical-intensity distribution in a thin layer of positive photoresist on a 31.75 mm square optical-grade fused quartz slide. First, each slide was chemically cleaned and layered with 1 μm of Shipley SC1813 positive photoresist using a SCS G3P8 Spin Coater. After a four-minute soft bake, each slide was exposed for 0.7 s with the PIIES configuration depicted in Fig. 6(b) and developed with a 30 s agitation bath of Microposit MF-319 Developer. The developed slides were evaluated initially using an Olympus NC60 microscope with a maximum of 100× magnification in the reflected light bright-field observation mode. Once the system was experimentally aligned and focused, the final exposed and developed slides were layered with 20 nm of Au/Pd using a Hummer 6 Gold Sputterer and imaged using a Zeiss Ultra60 scanning electron microscope (SEM). Detailed information concerning the PIIES configuration alignment, experimental

procedures, and instrumentation are in preparation and will be submitted for publication in a separate paper.

6. Single-Exposure Fabrication Results

Through careful experimental adjustment of the pattern-mask and sample-plane positions, the single-exposure PIIES aerial optical-intensity distribution was successfully recorded in the positive photoresist for two representative mask patterns presented here. First, a relatively large mask feature consisting of a 600.0 μm × 600.0 μm Greek cross as depicted in Fig. 7(a) was illuminated with the three off-axis interfering beams and projected to a size of 172.2 μm× 172.2 μm. The resulting optical-intensity distribution recorded in the photoresist is depicted in the SEM image of Fig. 7(b). Next, the model presented in Section 3, including the optical system parameters for the experimental configuration (see Appendix B), was used to predict the optical-intensity distribution for a corner of the projected cross as depicted in Fig. 7(c). Figure 7(d) depicts the magnified SEM view of the corresponding area of the fabricated PC structure, revealing the surrounding square PC lattice defined by black circular regions corresponding to the intensity maxima of the periodic pattern formed by the three interfering beams (grey areas indicate areas of intensity minima, while the white areas represent the transition between the points of maximum and minimum intensity). This simulation depicted in Fig. 7(c), with intensity grayscale values adjusted to match the SEM image, show very good agreement with the experimental results. In this first experiment, the cross successfully blocked all three beams, preventing the formation of the periodic interference pattern within the projected Greek cross, while transitioning to a well-defined PC lattice within the distance of one lattice constant, demonstrating PIIL's ability to define abrupt transitions within a PC lattice.

To demonstrate PIIL's ability to fabricate smaller PC structures, such as a single PC waveguide, a single line segment with mask dimensions of 2.0 μm × 20.0 μm as illustrated in Fig. 8(a) was illuminated with the three beams and projected to a size of 0.6 μm × 5.8 μm as depicted in the SEM image of Fig. 8(b). Figure 8(c) shows the simulated optical-intensity distribution for the PC lattice points near the projected waveguide segment. The corresponding magnified SEM view of the fabricated line segment is depicted in Fig. 8(d) showing the successful elimination of a single row of PC lattice points. Small deviations of the experimental optomechanical system from the perfectly aligned configuration used in

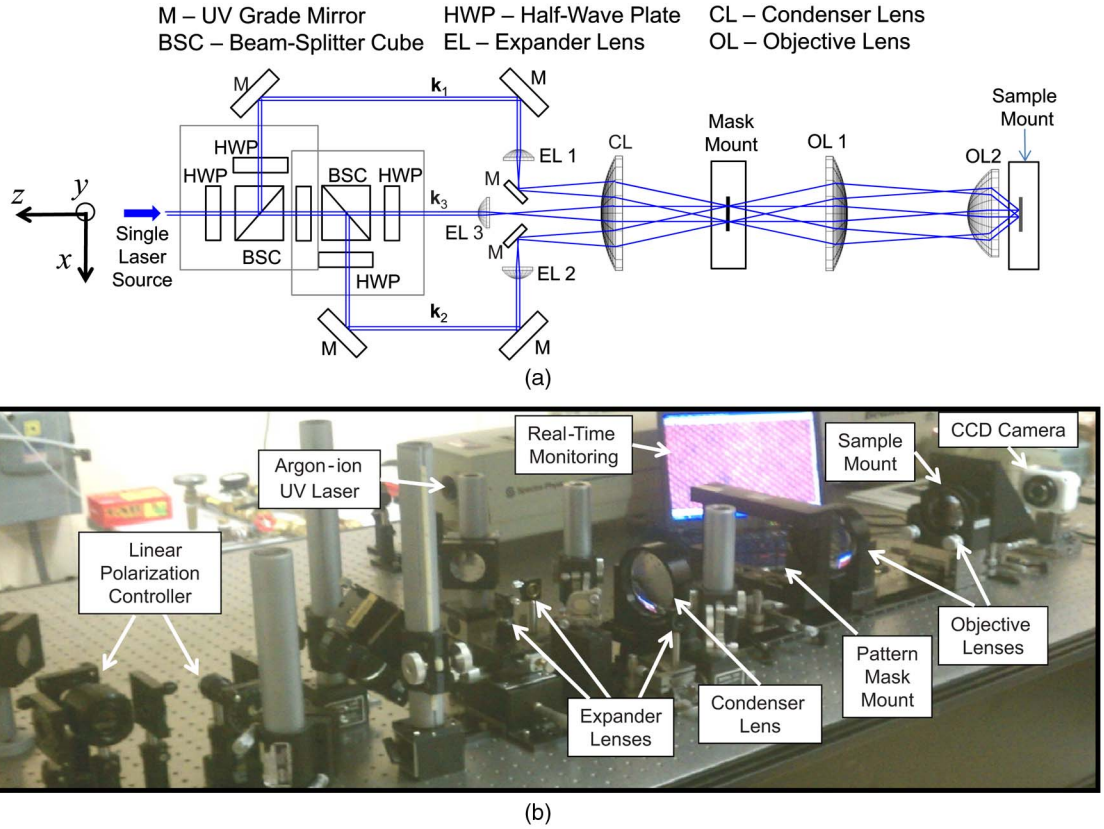

Fig. 6. (Color online) Experimental configuration. (a) The basic PIIES optical configuration includes the ability to set individually beam amplitudes and linear polarizations; (b) large diameter aspheric lenses are employed for the condenser and objective lenses in the laboratory implementation. Three-axis translational stages allow for precise placement of the mask features and sample plane to assist in focusing of the projected mask patterns.

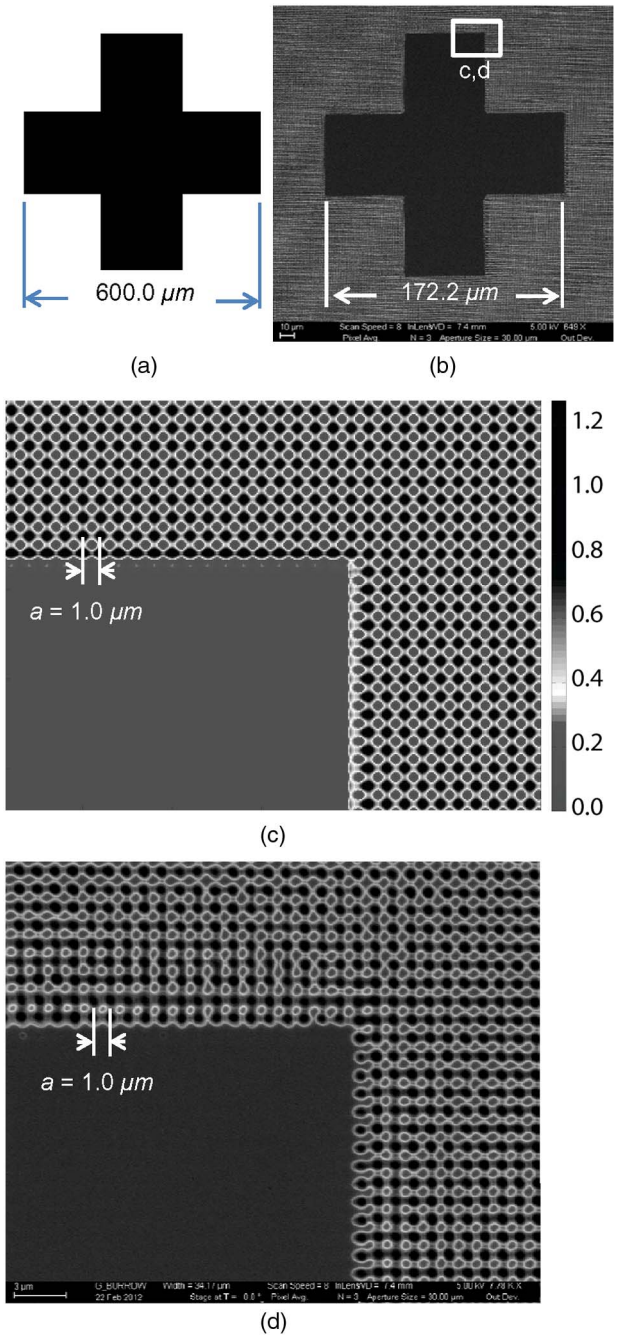

Fig. 7. (Color online) PIIES single-exposure fabrication results. (a) A pattern-mask feature of a 600.0 μm × 600.0 μm Greek cross is projected to a size of 172.2 μm × 172.2 μm; (b) an SEM image depicts the resulting single-exposure PIIES optical-intensity distribution of the projected cross and interference pattern; (c) a simulation provides a close-up view of one corner of the cross; (d) a magnified SEM view of the corresponding area depicts a well-defined corner produced by the projected Greek cross surrounded by the interferometrically defined square PC lattice with a periodicity of $a = 1.0$ μm.

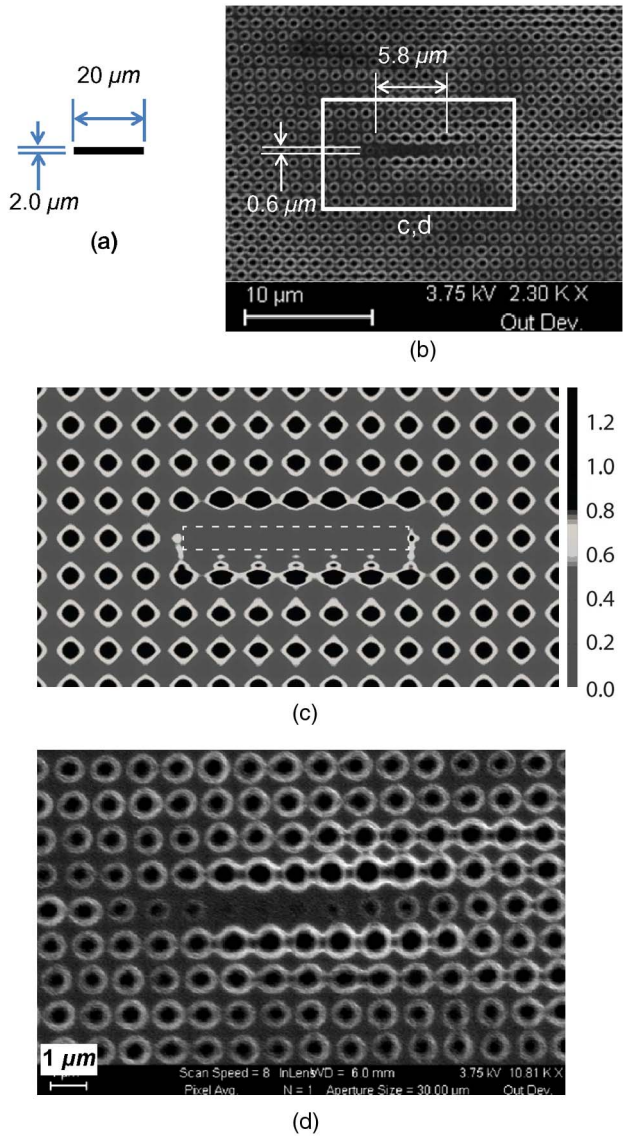

Fig. 8. (Color online) Demonstration of PIIL single-exposure PC waveguide fabrication. (a) A pattern-mask feature of a 2.0 μm × 20.0 μm line segment is projected to a size of 0.6 μm × 5.8 μm; (b) an SEM image depicts the resulting single-exposure PIIES optical-intensity distribution of the projected line segment and square-lattice PC; (c) a simulation depicts a close-up view of PC lattice points near the waveguide segment; (d) a magnified SEM view of the corresponding area depicts the selective elimination of a single row of lattice points in the surrounding periodic lattice, demonstrating the ability of the PIIL to fabricate a PC waveguide, the fundamental element of most PC devices.

the simulation may account for the qualitative differences between predicted and experimental results. Even with the optomechanical deviations present in the PIIES prototype, the experimental results presented in Fig. 8 demonstrate the ability of the PIIL to fabricate, in a single-exposure step, a PC waveguide, a fundamental structure in most PC devices. To the best of the authors' knowledge, this represents the first single-exposure fabrication of a basic PC waveguide structure using a combination of MBI patterning and high-spatial-frequency projection printing.

For the PIIES presented here, the total interference area is approximately 4 mm^2. Larger interference areas are possible as expander lens focal lengths are decreased, resulting in larger collimated interfering beam diameters at the sample plane.

From SEM images of the center and of the periphery of the interference area, the lattice constants were typically in the range from 1.02 μm to 1.06 μm. Lattice-vector angles for **a** and **b** varied typically by less than 1 deg. These results demonstrate excellent uniformity across the entire periodic pattern.

Based on Zemax simulations, the present PIIES configuration is capable of sub-500 nm periodicities with still smaller periodic features. In other PIIES experiments, lattice constants near 600 nm were achieved [42]. Of course, for smaller lattice periodicities, the required beam displacement d_{beam} depicted in Fig. 1(c) increases, placing the interfering beams near the limits of the clear apertures of the objective lenses. As a consequence, less of the diffracted energy from the projected mask features is collected by the objective lenses. This, in turn, degrades the quality of the projected mask features. For this reason, the beam displacements were adjusted to be well within the clear aperture limits of the objective lens to assist in focusing the projected mask features for the experimental results presented here. This resulted in a lattice periodicity of 1.0 μm. The initial fabrication results obtained with our relatively simple PIIES prototype and basic experimental procedures demonstrate the fundamental PIIL patterning capability. Future results are expected to be better with advanced systematic objective lens design (e.g., larger NA and reduced aberrations), improved optomechanical stability and alignment, and advanced lithographic processing techniques.

7. Discussion and Summary

With the *ad hoc* design and development of the PIIES, a novel three-beam interference system with an integrated projection imaging capability, the potential of PIIL for single-exposure fabrication of uniform PC lattices with integrated functional elements was demonstrated. In the prototype optical configuration presented here, only on-axis projection patterning was considered in order to demonstrate PIIL functionality. While rudimentary design considerations and experimental procedures were employed to minimize on-axis spherical aberration, no effort was made to minimize the off-axis aberrations. These aberrations will become significant in future design efforts to produce dense functional elements over a large area, especially considering the large-angle multibeam off-axis illumination required by the PIIES configuration. As described in previous work concerning traditional projection lithography [53], off-axis illumination requires detailed analysis of the diffracted energy in the objective lens pupil, with specific consideration given to reducing aberrations in order to image accurately both on- and off-axis mask features over a large area. These design considerations change with the pattern-mask feature size, shape, and density. In the PIIES configuration presented here, these same design considerations may be applied systematically to improve the optical configuration and allow for more precise modification of the interference pattern to create functional wafer-scale integrated optical circuits.

Interference patterning may be accomplished over a large area and is not greatly constrained by traditional diffraction limitations or depth of focus issues. However, this interferometric patterning capability does introduce new optical system design considerations. Specifically, to obtain a high-contrast uniform periodic optical-intensity distribution, the objective lens, in combination with the illumination optics, should be designed to produce a specific configuration of collimated interfering beams at the incidence angles required to produce the desired periodicity. The initial PIIL experimental results demonstrate that uniform interference patterning is consistently achieved even with the rudimentary optical configuration used here. Significantly larger interference areas with specific lattice symmetries are possible. Ongoing research and design efforts will be oriented to the optimization of PIIL.

With improved PIIES design and projection capability, the fundamental model presented here may be used to optimize pattern-mask designs, somewhat analogous to optical proximity correction. Recent research in this area suggests that, through proper mask feature design, the functional elements may be better defined by selective elimination of interference motifs, while minimizing the effects on the surrounding periodic pattern. This should improve the photonic bandgap characteristics of the PC lattice near the functional elements.

To expand PIIL application to the semiconductor industry and other nanoscale fabrication efforts, larger NA systems must be developed to reduce the minimum feature size. Accordingly, the scalar model presented here must be extended to cover high-NA effects and finite mask thicknesses. Specifically, the nonparaxial model must be modified to include polarization effects as NA values exceed 0.6 [50]. These polarization considerations will affect both the projected imaging and the periodic interference pattern. Fortunately, the same research and development of high-NA systems for the semiconductor industry should benefit the development of PIIL [54,55]. Fundamentally, higher NA systems will allow for larger incidence angles at the sample plane, corresponding to smaller period lattice patterns. With the reduced period, smaller projected mask features will be required. Of course, higher-NA systems will facilitate accomplishing this. It is anticipated that the resolution limits of the PIIL method will be similar to those of traditional projection lithography, with two possible key exceptions, (1) the diffraction-limited imaging resolution may be reduced since the high-spatial-frequency patterning is formed by mask-less MBI, and (2) the projected mask features need only modify the interference pattern, possibly reducing the required effective resolution of the integrated imaging system.

In conclusion, the research and initial results presented here confirm the potential of PIIL for

single-exposure fabrication of PC lattices with integrated functional elements using a PIIES configuration. With future research, improved optical system design, and additional processing considerations, PIIL holds the promise of commercially cost-effective wafer-scale fabrication of dense integrated optical circuits. While the current research has focused on the demonstration and fabrication of PC structures, PIIL and future PIIES designs have the potential to impact an increasingly wide variety of application areas including nano-electronics, biomedical structures, optical trapping, and numerous other subwavelength structures.

Appendix A

To simulate the PIIES optical-intensity distribution using the model presented in Section 3, representative optical system parameters are needed. The accuracy of the model depends on these parameters, specifically the Zernike fringe coefficients. For well-corrected systems with small Zernike fringe coefficients, aberrations are minimized, and the projected image quality is limited primarily by the ability of the objective lens system to collect the diffracted light from the mask. For Figs. 2–5 in Sections 3 and 4, Zemax models and manufacturer lens specifications were used to obtain the system parameters for the projection system formed by objective lens 1 (Thorlabs AL100200-B) and objective lens 2 (Thorlabs AL7560-A). All illuminating beams were assumed to be collimated and modeled as coherent plane waves. The common incidence angle θ_M and azimuthal angles φ_i of each illuminating beam were optimized in Zemax to produce the desired wave vector configuration at the sample as required for a lattice constant of 600 nm and a square translational symmetry oriented as depicted in Fig. 1(b). Individual beam linear polarizations were selected to produce $p4m$ plane group symmetry. The resulting parameters for the objective lens system used in the simulations for PC waveguide coupler depicted in Figs. 2–5 are given in Table A1. The Zemax-derived values for the Zernike fringe coefficients at the design wavelength of 780 nm are given in Table A2. These values provide coefficients consistent with the literature and are representative of the values that should be possible for the same lenses, corrected for the UV wavelength of 363.8 nm used in the present work.

Table A1. Objective Lens Parameters for PC Waveguide Coupler in Figs. 2–5

Parameter	Value
λ	363.8 nm
$\mathbf{k}_1$	$2\pi/\lambda(-0.30, -0.30, -0.90)$
$\mathbf{k}_2$	$2\pi/\lambda(0.30, -0.30, -0.90)$
$\mathbf{k}_3$	$2\pi/\lambda(-0.30, 0.30, -0.90)$
$\hat{\mathbf{e}}_1$	(–0.44, 0.81, 0.38)
$\hat{\mathbf{e}}_2$	(–0.89, 0.18, 0.42)
$\hat{\mathbf{e}}_3$	(0.25, 0.96, 0.12)
θ_M	7.24 deg
φ_i	$(45, 135, -45)$ deg
f_2	56.87 mm
CA_2	57.73 mm
$\lvert m\rvert$	0.30

Table A2. Zernike Fringe Coefficients for PC Waveguide Coupler in Figs. 2–5

Zernike Fringe Coefficient	Value (nm)
Z_1	11.33
Z_4	8.57
Z_9	–7.16
Z_{16}	–0.89
Z_{25}	1.34
Z_{36}	–1.80
Z_{37}	0.41

Appendix B

To simulate the experimental optical-intensity distributions for comparison with the fabrication results for the Greek cross and line segments depicted in Figs. 7 and 8, Zemax was again used to obtain the system parameters for the projection system as described in Appendix A. However, to match the experimental configuration, the common incidence angle θ_M of each illuminating beam was optimized for a lattice constant of 1.0 μm. The resulting parameters for the objective lens system used in the simulations for Figs. 7 and 8 are given in Table B1.

To provide an accurate prediction of the optical-intensity distribution for the experimental configuration, the Zemax Zernike fringe coefficients were

Table B1. Objective Lens Parameters for the Greek Cross and Line Segments in Figs. 7 and 8

Parameter	Value
λ	363.8 nm
$\mathbf{k}_1$	$2\pi/\lambda(-0.18, -0.18, -0.97)$
$\mathbf{k}_2$	$2\pi/\lambda(0.18, -0.18, -0.97)$
$\mathbf{k}_3$	$2\pi/\lambda(-0.18, 0.18, -0.97)$
$\hat{\mathbf{e}}_1$	(–0.48, 0.85, 0.22)
$\hat{\mathbf{e}}_2$	(–0.26, 0.96, 0.07)
$\hat{\mathbf{e}}_3$	(0.94, 0.23, 0.25)
θ_M	4.42 deg
φ_i	$(45, 135, -45)$ deg
f_2	56.87 mm
CA_2	57.73 mm
$\lvert m\rvert$	0.30

Table B2. Zernike Fringe Coefficients for the Greek Cross and Line Segments in Figs. 7 and 8

Zernike Fringe Coefficient	Value (nm)
Z_1	172.86
Z_4	126.87
Z_9	384.16
Z_{16}	499.95
Z_{25}	71.16
Z_{36}	2.65
Z_{37}	1.36

obtained for a source wavelength of 363.8 nm and are listed in Table B2. These values are generally an order of magnitude larger than those given in Table A2. This is due to the fact that the lenses were designed for a wavelength of 780 nm. The UV source used in the PIIES prototype resulted in the increased Zernike fringe coefficient values and provided a more accurate model for comparison to experimental results.

This work was supported in part by grant no. ECCS 0925119 from the National Science Foundation.

References

1. G. M. Burrow and T. K. Gaylord, "Multi-beam interference advances and applications: nano-electronics, photonic crystals, metamaterials, subwavelength structures, optical trapping, and biomedical structures," Micromachines **2**, 221–257 (2011).
2. D. Xia, Z. Ku, S. C. Lee, and S. R. J. Brueck, "Nanostructures and functional materials fabricated by interferometric lithography," Adv. Mater. **23**, 147–179 (2011).
3. M. Fritze, T. M. Bloomstein, B. Tyrrell, T. H. Fedynyshyn, N. N. Efremow, Jr., D. E. Hardy, S. Cann, D. Lennon, S. Spector, M. Rothschild, and P. Brooker, "Hybrid optical maskless lithography: scaling beyond the 45 nm node," J. Vac. Sci. Technol. B **23**, 2743–2748 (2005).
4. M. C. Lemme, C. Moormann, H. Lerch, M. Moller, B. Vratzov, and H. Kurz, "Triple-gate metal-oxide-semiconductor field effect transistors fabricated with interference lithography," Nanotechnol. **15**, 208–210 (2004).
5. R. T. Greenway, R. Hendel, K. Jeong, A. B. Kahng, J. S. Petersen, Z. Rao, and M. C. Smayling, "Interference assisted lithography for patterning of 1D gridded design," Proc. SPIE **7271**, 72712U (2009).
6. V. Berger, O. Gauthier-Lafaye, and E. Costard, "Fabrication of a 2D photonic bandgap by a holographic method," Electron. Lett. **33**, 425–426 (1997).
7. M. Campbell, D. N. Sharp, M. T. Harrison, R. G. Denning, and A. J. Turberfield, "Fabrication of photonic crystals for the visible spectrum by holographic lithography," Nature **404**, 53–56 (2000).
8. R. C. Rumpf and E. G. Johnson, "Fully three-dimensional modeling of the fabrication and behavior of photonic crystals formed by holographic lithography," J. Opt. Soc. Am. A **21**, 1703–1713 (2004).
9. N. Feth, C. Enkrich, M. Wegener, and S. Linden, "Large-area magnetic metamaterials via compact interference lithography," Opt. Express **15**, 501–507 (2007).
10. Y. Yang, Q. Z. Li, and G. P. Wang, "Design and fabrication of diverse metamaterial structures by holographic lithography," Opt. Express **16**, 11275–11280 (2008).
11. D. Sawaki and J. Amako, "Deep-UV laser-based nanopatterning with holographic techniques," Proc. SPIE **6459**, 64590F (2007).
12. J. P. Spallas, A. M. Hawryluk, and D. R. Kania, "Field emitter array mask patterning using laser interference lithography," J. Vac. Sci. Technol. B **13**, 1973–1978 (1995).
13. C. H. Liu, M. H. Hong, H. W. Cheung, F. Zhang, Z. Q. Huang, L. S. Tan, and T. S. A. Hor, "Bimetallic structure fabricated by laser interference lithography for tuning surface plasmon resonance," Opt. Express **16**, 10701–10709 (2008).
14. M. Duarte, A. Lasagni, R. Giovanelli, J. Narciso, E. Louis, and F. Mucklich, "Increasing lubricant film lifetime by grooving periodical patterns using laser interference metallurgy," Adv. Eng. Mater. **10**, 554–558 (2008).
15. R. Murillo, H. A. van Wolferen, L. Abelmann, and J. C. Lodder, "Fabrication of patterned magnetic nanodots by laser interference lithography," Microelectron. Eng. **78–79**, 260–265 (2005).
16. E. Schonbrun, R. Piestun, P. Jordan, J. Cooper, K. D. Wulff, J. Courtial, and M. Padgett, "3D interferometric optical tweezers using a single spatial light modulator," Opt. Express **13**, 3777–3786 (2005).
17. A. E. Chiou, W. Wang, G. J. Sonek, J. Hong, and M. W. Berns, "Interferometric optical tweezers," Opt. Commun. **133**, 7–10 (1997).
18. P. Jakl, T. Cizmar, M. Sery, and P. Zemanek, "Static optical sorting in a laser interference field," Appl. Phys. Lett. **92**, 161110 (2008).
19. E. L. Hedberg-Dirk and U. A. Martinez, "Large-scale protein arrays generated with interferometric lithography for spatial control of cell-material interactions," J. Nanomater. **2010**, 176750 (2010).
20. J.-H. Jang, D. Dendukuri, H. T. Alan, E. L. Thomas, and P. S. Doyle, "A route to three-dimensional structures in a microfluidic device: stop-flow interference lithography," Ang. Chem. Int. Ed. **46**, 9027–9031 (2007).
21. F. A. Zoller, C. Padeste, Y. Ekinci, H. H. Solak, and A. Engel, "Nanostructured substrates for high density protein arrays," Microelectron. Eng. **85**, 1370–1374 (2008).
22. G. M. Burrow and T. K. Gaylord, "Constrained parametric optimization of point geometries in multi-beam-interference lithography," in *Frontiers in Optics*, OSA Technical Digest (CD) (Optical Society of America, 2010), paper FWS3.
23. L. Z. Cai, X. L. Yang, and Y. R. Wang, "All fourteen Bravais lattices can be formed by interference of four noncoplanar beams," Opt. Lett. **27**, 900–902 (2002).
24. A. I. Petsas, A. B. Coates, and G. Grynberg, "Crystallography of optical lattices," Phys. Rev. A **50**, 5173–5189 (1994).
25. L. J. Wu, Y. C. Zhong, K. S. Wong, G. P. Wang, and L. Yuan, "Fabrication of hetero-binary and honeycomb photonic crystals by one-step holographic lithography," Appl. Phys. Lett. **88**, 091115 (2006).
26. L. Z. Cai, X. L. Yang, and Y. R. Wang, "Interference of three noncoplanar beams: patterns, contrast and polarization optimization," J. Mod. Opt. **49**, 1663–1672 (2002).
27. J. L. Stay and T. K. Gaylord, "Conditions for primitive-lattice-vector-direction equal contrasts in four-beam-interference lithography," Appl. Opt. **48**, 4801–4813 (2009).
28. L. Z. Cai, X. L. Yang, and Y. R. Wang, "Formation of a microfiber bundle by interference of three noncoplanar beams," Opt. Lett. **26**, 1858–1860 (2001).
29. J. L. Stay and T. K. Gaylord, "Three-beam-interference lithography: contrast and crystallography," Appl. Opt. **47**, 3221–3230 (2008).
30. N. D. Lai, J. H. Lin, W. P. Liang, C. C. Hsu, and C. H. Lin, "Precisely introducing defects into periodic structures by using a double-step laser scanning technique," Appl. Opt. **45**, 5777–5782 (2006).
31. T. Liu, M. Fallahi, J. V. Moloney, and M. Mansuripur, "Fabrication of two-dimensional photonic crystals with embedded defects using blue-laser-writer and optical holography," IEEE Photon Technol. Lett. **18**, 1100–1102 (2006).
32. J. Murakowski, G. J. Schneider, and D. Prather, "Fabrication of 3-dimensional photonic crystals with embedded defects," Proc. SPIE **5347**, 181–189 (2004).
33. P. Parisse, D. Luciani, A. D'Angelo, S. Santucci, P. Zuppella, P. Tucceri, A. Reale, and L. Ottaviano, "Patterning at the nanoscale: atomic force microscopy and extreme ultraviolet interference lithography," Mater. Sci. Eng. B **165**, 227–230 (2009).
34. C. J. M. van Rijn, "Laser interference as a lithographic nanopatterning tool," J. Microlith. Microfab. Microsyst. **5**, 011012 (2006).
35. B. D. Gates, Q. Xu, M. Stewart, D. Ryan, C. G. Willson, and G. M. Whitesides, "New approaches to nanofabrication: molding, printing, and other techniques," Chem. Rev. **105**, 1171–1196 (2005).
36. B. W. Smith, "Alternative optical technologies: more than curiosities?" Proc. SPIE **7274**, 21–210 (2009).
37. T. Jhaveri, A. Strojwas, L. Pileggi, and V. Rovner, "Economic assessment of lithography strategies for the 22 nm technology node," Proc. SPIE **7488**, 74882Y (2009).
38. N. D. Lai, W. P. Liang, J. H. Lin, and C. C. Hsu, "Rapid fabrication of large-area periodic structures containing well-defined defects by combining holography and mask techniques," Opt. Express **13**, 5331–5337 (2005).
39. Y. K. Lin, A. Harb, K. Lozano, D. Xu, and K. P. Chen, "Five beam holographic lithography for simultaneous fabrication

of three dimensional photonic crystal templates and line defects using phase tunable diffractive optical element," Opt. Express **17**, 16625–16631 (2009).
40. C. A. Mack, *Field Guide to Optical Lithgraphy* (SPIE, 2006).
41. G. M. Burrow and T. K. Gaylord, "Apparatus and method for photolithographic projection exposure for fabrication of one-, two-, and three-dimensional periodic structures with or without integrated patterns," U.S. patent application 13/249,841 (30 September 2011).
42. G. M. Burrow and T. K. Gaylord, "Interference projection exposure system," in *Frontiers in Optics*, OSA Technical Digest (CD) (Optical Society of America, 2011), paper FWZ2.
43. G. M. Burrow and T. K. Gaylord, "Diffractive photo-mask for production of non-periodic functional elements integrated within periodic lattices and method for making the same," U.S. patent application 13/250,011 (30 September 2011).
44. S. Boscolo, M. Midrio, and C. G. Someda, "Coupling and decoupling of electromagnetic waves in parallel 2D photonic-crystal waveguides," IEEE J. Quantum Electron. **38**, 47–53 (2002).
45. A. K.-K. Wong, *Optical Imaging in Projection Microlithography* (SPIE Optical Engineering, 2005).
46. J. L. Stay and T. K. Gaylord, "Contrast in four-beam-interference lithography," Opt. Lett. **33**, 1434–1436 (2008).
47. J. R. Sheats and B. W. Smith, *Microlithography: Science and Technology* (Marcel Dekker, 1998).
48. M. Born and E. Wolf, *Principles of Optics*, 6th ed. (Pergamon, 1980).
49. *Zemax Optical Design Program User's Guide* (Focus Software, Inc., 2003).
50. D. C. Cole, E. Barouch, U. Hollerbach, and S. A. Orszag, "Derivation and simulation of higher numerical aperture scalar aerial images," Jpn. J. Appl. Phy. **31**, 4110–4119 (1992).
51. MATLAB R2008a (The Mathworks, Natick, Massachusetts).
52. J. L. Stay, G. M. Burrow, and T. K. Gaylord, "Three-beam interference lithography methodology," Rev. Sci. Instrum. **82**, 023115 (2011).
53. B. W. Smith and R. Schlief, "Understanding lens aberration and influences on lithographic imaging," Proc. SPIE **4000**, 294–306 (2000).
54. D. G. Flagello, T. Milster, and A. E. Rosenbluth, "Theory of high-NA imaging in homogeneous thin films," J. Opt. Soc. Am. A **13**, 53–64 (1996).
55. M. Totzeck, P. Graupner, T. Heil, A. Gohnermeier, O. Dittmann, D. Krahmer, V. Kamenov, J. Ruoff, and D. Flagello, "Polarization influence on imaging," J. Microlith. Microfab. Microsyst. **4**, 031108 (2005).